# Accelerated monotonic convergence of optimal control over quantum dynamics

Tak-San Ho* and Herschel Rabitz†
*Department of Chemistry, Princeton University, Princeton, New Jersey 08544, USA*
(Received 22 December 2009; revised manuscript received 21 May 2010; published 12 August 2010)

The control of quantum dynamics is often concerned with finding time-dependent optimal control fields that can take a system from an initial state to a final state to attain the desired value of an observable. This paper presents a general method for formulating monotonically convergent algorithms to iteratively improve control fields. The formulation is based on a two-point boundary-value quantum control paradigm (TBQCP) expressed as a nonlinear integral equation of the first kind arising from dynamical invariant tracking control. TBQCP is shown to be related to various existing techniques, including local control theory, the Krotov method, and optimal control theory. Several accelerated monotonic convergence schemes for iteratively computing control fields are derived based on TBQCP. Numerical simulations are compared with the Krotov method showing that the new TBQCP schemes are efficient and remain monotonically convergent over a wide range of the iteration step parameters and the control pulse lengths, which is attributable to the trap-free character of the transition probability quantum dynamics control landscape.

DOI: 10.1103/PhysRevE.82.026703 PACS number(s): 02.60.Pn

## I. INTRODUCTION

A common quantum control objective is to drive a system from a given initial state to a final state that maximizes the expectation value of a particular observable. In recent years, much progress in the quantum control field has been made by drawing on powerful computers and state-of-the art laser pulse shaping technologies [1] as well as optimal control theory (OCT) [2–6], including stochastic-based genetic algorithms (GA) [7–10], local control theory (LCT) [11–17], and the diffeomorphic modulation under observable-response-preserving homotopy (D-MORPH) method [18–20]. The OCT and LCT methods have provided the machinery for the development of many practical computational algorithms for simulating a variety of quantum control problems. In the laboratory, a GA is frequently employed to guide the closed-loop adaptive search for optimal control fields [21].

A main challenge for quantum optimal control simulations is dealing with the iterative process of searching for time dependent control fields. The number of required iterations can render the OCT- and GA-based methods computationally formidable for control problems involving just a few degrees of freedom. Much effort has gone into developing efficient schemes to meet these intense computational demands, including the quadratically convergent conjugate-gradient (CG) method [22], rapid monotonically convergent iteration algorithms [4,23–31]—especially the Krotov method [23–25], the Zhu-Rabitz algorithm [27,28] and its variants [29,30], and the recently developed D-MORPH gradient-based searching technique [18–20]. The efficacy of these approaches can be attributed to the general trap-free nature of general optimal control landscape features [32–35]. Among these methods, the D-MORPH method is particularly useful for exploring quantum control landscapes [18]. Monotonically convergent schemes have also been proposed to solve quantum optimal control problems described by integro-differential equations of motion [36] and to involve nonlinear interactions [37,38].

For any control design method a key objective is to reach the target state with the smallest possible computational effort. In addition to seeking iteration-to-iteration monotonicity, the monotonic convergence property would be attractive to retain at every instant of time throughout the evolution [31], which is a manifestation of LCT [11–17] and many of monotonic convergence algorithms [31]. Recently, a general intuitive formulation of LCT was developed in the context of Lyapunov-type functions [16,17] in terms of a performance index that tracks the so-called dynamical invariants [39] (Sec. II below provides an explicit definition of a dynamical invariant) of the field-free Hamiltonian [16]. This technique was further extended by tracking the dynamical invariants associated with a reference control field to facilitate the computation of the desired control field [17]. The LCT procedure is related to inverse tracking control methods [40–44] which allow for the construction of a control field on the fly from one time step to the next. Although the LCT method is computationally attractive, it is generally difficult to determine the length of time needed to steer a quantum system to the desired state [17]. Toward this end, a promising monotonically convergent iterative scheme has been proposed recently [17] drawing on the prospect of generating short intense pulses [14,15,17].

This paper presents the control of quantum systems as a two-point boundary-value quantum control paradigm (TBQCP) based on a nonlinear integral equation of the first kind. The integral equation arises from the Heisenberg equation of motion for tracking a dynamical invariant [39] associated with the observable. A self-consistent solution of this nonlinear integral equation coincides with the LCT formulation for the control field. TBQCP provides new insights into many existing monotonically convergent iteration techniques, particularly the Krotov method. In addition, TBQCP and OCT are related in that the latter involves the dynamical invariant belonging to the observable in the variational OCT cost functional. This paper shows that the TBQCP frame-

*tsho@princeton.edu
†hrabitz@princeton.edu

 

work can be employed to develop efficient and robust algorithms for seeking optimal control fields.

Section II of the paper presents the TBQCP formulation. Section III compares TBQCP and Krotov algorithms. Section IV describes the relationship between TBQCP and the variational OCT formulation. In Sec. V various accelerated TBQCP monotonically convergent schemes are proposed for iterative computation of control fields. Numerical simulations corresponding to two significantly different control pulse lengths are presented in Sec. VI using a model of the OH diatom. Comparisons are made between various TBQCP schemes and the Krotov method, based on initial reference control fields, one from LCT and another given as a linearly chirped field. Finally, a short summary of the work is given in Sec. VII.

## II. GENERAL FORMULATION

The TBQCP algorithm addresses the objective of finding a control field $E(t)$ to steer a quantum system from an initial state $|\psi(0)\rangle$ to a final state $|\psi(T)\rangle$ at time $T$ so as to attain the desired expectation value $\langle O(T)\rangle \equiv \langle\psi(T)|O(T)|\psi(T)\rangle$ of a time-dependent Hermitian operator (observable) $O(t)$. The state wave function $|\psi(t)\rangle$ evolves according to the time-dependent Schrödinger equation

$$\frac{\partial}{\partial t}|\psi(t)\rangle = \frac{1}{\imath\hbar}\{H_0 - \mu E(t)\}|\psi(t)\rangle, \tag{1}$$

and can be cast as

$$|\psi(t)\rangle = U(t,0)|\psi(0)\rangle, \tag{2}$$

where

$$\frac{\partial}{\partial t}U(t,0) = \frac{1}{\imath\hbar}\{H_0 - \mu E(t)\}U(t,0), \quad U(0,0) = \mathbf{I}. \tag{3}$$

The expectation value $\langle O(t)\rangle$ is defined as

$$\langle O(t)\rangle \equiv \langle\psi(t)|O(t)|\psi(t)\rangle. \tag{4}$$

Here $H_0$ and $\mu$ are, respectively, the field-free Hamiltonian and dipole moment operator. In this paper, we consider tracking a positive semidefinite explicitly time-dependent (dynamical) invariant $O(t)$ (i.e., $\langle O(t)\rangle \geq 0$, $dO(t)/dt = 0$ and $O^\dagger(t) = O(t)\,\forall\, t \in [0,T]$) associated with a reference control field $E^{(0)}(t)$ and satisfying the invariant equation [39].

$$\frac{dO(t)}{dt} \equiv \frac{\partial}{\partial t}O(t) + \frac{1}{\imath\hbar}[O(t), H_0 - \mu E^{(0)}(t)] = 0, \quad O(T) = O_T, \tag{5}$$

where $O(T)$ is chosen to coincide with a specific physical observable operator $O_T$ of interest. From Eq. (5), the dynamical invariant $O(t)$ can be formally written as

$$O(t) = U_0(t,T)O_T U_0^\dagger(t,T), \tag{6}$$

where the propagator $U_0(t,T)$ is governed by the backward propagated time-dependent Schrödinger equation

$$\frac{\partial}{\partial t}U_0(t,T) = \frac{1}{\imath\hbar}\{H_0 - \mu E^{(0)}(t)\}U_0(t,T), \quad U_0(T,T) = \mathbf{I}. \tag{7}$$

From Eq. (6) and the state $|\psi^{(0)}(t)\rangle \equiv U_0(t,0)|\psi(0)\rangle$, it can be shown that the following expectation value,

$$\begin{aligned}\langle\psi^{(0)}(t)|O(t)|\psi^{(0)}(t)\rangle &= \langle\psi^{(0)}(t)|U_0(t,T)O(T)U_0(T,t)|\psi^{(0)}(t)\rangle \\ &= \langle\psi^{(0)}(T)|O(T)|\psi^{(0)}(T)\rangle \\ &= \langle\psi(0)|O(0)|\psi(0)\rangle,\end{aligned} \tag{8}$$

is independent of the time $t$, i.e., $d\langle\psi^{(0)}(t)|O(t)|\psi^{(0)}(t)\rangle/dt = 0$. Taking the time derivative of Eq. (4) renders the Heisenberg equation of motion

$$\begin{aligned}\frac{d}{dt}\langle O(t)\rangle &\equiv \frac{d}{dt}\langle\psi(t)|O(t)|\psi(t)\rangle \\ &= \langle\psi(t)|-\frac{1}{\imath\hbar}[H_0, O(t)] + \frac{\partial O(t)}{\partial t}|\psi(t)\rangle \\ &\quad + \langle\psi(t)|\frac{1}{\imath\hbar}[\mu, O(t)]|\psi(t)\rangle E(t).\end{aligned} \tag{9}$$

After invoking Eq. (5), then Eq. (9) can be manipulated into a simple equation

$$\frac{d}{dt}\langle O(t)\rangle = f_\mu(t)\{E(t) - E^{(0)}(t)\}, \tag{10}$$

where

$$f_\mu(t) \equiv \langle\psi(t)|\frac{1}{\imath\hbar}[\mu, O(t)]|\psi(t)\rangle = -\frac{2}{\hbar}\mathrm{Im}\{\langle\psi(t)|O(t)\mu|\psi(t)\rangle\}, \tag{11}$$

is a functional of the control field $E(t)$ and of the reference field $E^{(0)}(t)$, since, as shown in Eq. (8), $O(t)$ is a dynamical invariant associated with the control field $E^{(0)}(t)$, cf. Eq. (5). Here "Im" denotes the imaginary part. Integrating Eq. (10) produces the nonlinear integral equation

$$\langle O(T)\rangle - \langle O(0)\rangle = \int_0^T f_\mu(t)\{E(t) - E^{(0)}(t)\}dt, \tag{12}$$

where

$$\langle O(T)\rangle = \langle\psi(T)|O_T|\psi(T)\rangle = \langle\psi(0)|U(0,T)O_T U(T,0)|\psi(0)\rangle$$

is a functional of the control field $E(t)$ and $\langle O(0)\rangle = \langle\psi(0)|O(0)|\psi(0)\rangle = \langle\psi(0)|U_0(0,T)O_T U_0(T,0)|\psi(0)\rangle$ is a functional of $E^{(0)}(t)$.

Equations (1), (5), and (12) form the TBQCP for computing the desired control field $E(t)$: Given the expectation value $\langle O(T)\rangle$ of a dynamical invariant $O(t)$ associated with an arbitrarily chosen reference control field $E^{(0)}(t)$ and the initial

state $|\psi(0)\rangle$ of the quantum system, a solution $E(t)$ of Eq. (12) is sought by iteratively integrating Eq. (1) forward and Eq. (5) backward over the interval $[0,T]$. To this end, a self-consistent solution to Eq. (12) may be formally cast as

$$E(t) - E^{(0)}(t) = S(t)\{\epsilon(t) - \epsilon^{(0)}(t)\} = \eta S(t)[f_\mu(t) + f_\perp(t)], \tag{13}$$

where $S(t)$ is the control field envelope function $S(t) \geq 0$ [such that $E(t) = S(t)\epsilon(t)$ and $E^{(0)}(t) = S(t)\epsilon^{(0)}(t)$], $\eta$ is defined as

$$\eta \equiv \frac{\langle O(T)\rangle - \langle O(0)\rangle}{\int_0^T S(t)[f_\mu(t)]^2 dt}. \tag{14}$$

and $f_\perp(t)$ is a function of time in the null space of $f_\mu(t)$, i.e.,

$$\int_0^T S(t) f_\mu(t) f_\perp(t) dt = 0. \tag{15}$$

Although a nonzero function $f_\perp(t)$ in principle can only be determined *post facto* (i.e., after $f_\mu(t)$ is computed over the whole time interval $[0,T]$), in practice it can be chosen by approximating $f_\mu(t)$ from earlier iterations. Moreover, the expectation value $\langle O(T)\rangle$, which depends on $E(t)$, thus on the value of $\eta$ and the function $f_\perp(t)$ via Eq. (13), in general cannot be determined *a priori*; as a result, the parameter $\eta$ can be judiciously chosen initially as a positive number $\eta > 0$ such that $\langle O(T)\rangle > \langle O(0)\rangle$. From Eq. (15), it can be shown that the square norm $\|E - E^{(0)}\|^2$ is bounded by the relation:

$$\begin{aligned}\frac{\|E - E^{(0)}\|^2}{\eta^2} &\equiv \frac{1}{\eta^2}\int_0^T S(t)[\epsilon(t) - \epsilon^{(0)}(t)]^2 dt \\ &= \int_0^T S(t)[f_\mu(t)]^2 dt + \int_0^T S(t)[f_\perp(t)]^2 dt \\ &\geq \int_0^T S(t)[f_\mu(t)]^2 dt. \end{aligned} \tag{16}$$

The equal sign in Eq. (16) holds when $f_\perp(t) = 0$, corresponding to the minimum norm for the difference $E(t) - E^{(0)}(t)$. Equations. (13) and (15) can be succinctly recast as

$$E(t) - E^{(0)}(t) = \eta S(t)\{(1 - \zeta) f_\mu(t) + f(t)\}, \tag{17}$$

where $f(t)$ may be zero or a nonzero function of time $t$, $t \in [0,T]$, and

$$\zeta \equiv \frac{\int_0^T S(t) f_\mu(t) f(t) dt}{\int_0^T S(t)[f_\mu(t)]^2 dt}, \tag{18}$$

which in practice may be approximated using $f_\mu(t)$ from the preceding iteration by noting that $f_\perp(t) = f(t) - \zeta f_\mu(t)$. Using Eq. (17) in Eq. (12) leads to

$$\begin{aligned}\langle O(T)\rangle - \langle O(0)\rangle &= \eta \int_0^T S(t) f_\mu(t)\{(1 - \zeta) f_\mu(t) + f(t)\} dt \\ &= \eta \int_0^T S(t)[f_\mu(t)]^2 dt \geq 0. \end{aligned} \tag{19}$$

For $\eta > 0$, and using Eqs. (8) and (19), the following inequality holds

$$\begin{aligned}&\langle \psi(T)|O(T)|\psi(T)\rangle \\ &\quad \geq \langle \psi(0)|O(0)|\psi(0)\rangle \\ &\quad = \langle \psi(0)|U_0(0,T)O(T)U_0(T,0)|\psi(0)\rangle \\ &\quad = \langle \psi^{(0)}(0)|U_0(0,T)O(T)U_0(T,0)|\psi^{(0)}(0)\rangle \\ &\quad = \langle \psi^{(0)}(T)|O(T)|\psi^{(0)}(T)\rangle, \end{aligned} \tag{20}$$

regardless of the temporal behavior of $E(t)$ and $E^{(0)}(t)$. Equations. (2), (5), (10), (11), (17), and (18) are the basic relations for implementing TBQCP.

Equations (10), (11), (17), (19), and (20) can be readily exploited to attain various monotonically convergent procedures for determining the control field. In particular, for the special case of $f_\perp(t) = 0$, Eq. (17) reduces to the LCT in Ref. [17].

$$E(t) = E^{(0)}(t) + \eta S(t) f_\mu(t) \tag{21}$$

and we readily obtain the LCT characteristic

$$\frac{d}{dt}\langle O(t)\rangle|_{f(t)=0} = \eta S(t)[f_\mu(t)]^2 \geq 0. \tag{22}$$

It can be shown in this case that the norm $\|E\|$ is bounded by the Minkowski's integral inequality

$$\begin{aligned}\frac{\|E\|}{\eta} &\equiv \sqrt{\int_0^T S(t)[\epsilon(t)]^2 dt} \\ &\leq \sqrt{\int_0^T S(t)[\epsilon^{(0)}(t)]^2 dt} + \sqrt{\int_0^T S(t)[f_\mu(t)]^2 dt}. \end{aligned}$$

Equations (20) and (22) guarantee that the iterative scheme (i.e., the Mirrahimi-Turinici-Rouchon algorithm [17]) based on the recurrence relation

$$E^{(n)}(t) = E^{(n-1)}(t) + \eta S(t) f_\mu(t), \quad n = 1,2,\ldots, \tag{23}$$

is monotonically convergent not only from iteration to iteration, but also throughout the time evolution. The function $f_\mu(t)$, defined in Eq. (11), is evaluated for the control field $E(t) = E^{(n)}(t)$ and the reference field $E^{(0)}(t) = E^{(n-1)}(t)$ at the $n$th iteration (for practical implementation, see Sec. VI). For the general case of $f_\perp(t) \neq 0$, we have instead $f(t) \neq 0$ in Eq. (17). In this case, substituting Eq. (17) in Eq. (10) results in

$$\frac{d}{dt}\langle O(t)\rangle\big|_{f(t)\neq 0} = \eta S(t)\{(1-\zeta)[f_\mu(t)]^2 + f_\mu(t)f(t)\}, \quad (24)$$

which may be further manipulated for accelerating the convergence of $\langle O(t)\rangle$ toward the target value $\langle O(T)\rangle$ over time. In principle, the free function $f(t)$ in Eq. (24) may be chosen to satisfy

$$q(t) \equiv -\zeta[f_\mu(t)]^2 + f_\mu(t)f(t) \geq 0 \quad \forall\, t \in [0,T] \quad (25)$$

such that the relation

$$\frac{d}{dt}\langle O(t)\rangle\big|_{f(t)\neq 0} \geq \frac{d}{dt}\langle O(t)\rangle\big|_{f(t)=0} \quad (26)$$

holds over time. In practice, the sign of the function $q(t)$ will alternate over the time interval $[0,T]$ and may be kept predominantly positive throughout, for example, by choosing $f(t)$ such that the parameter satisfies $\zeta<0$ in Eq. (25), or equivalently the *acceleration* parameter becomes $(1-\zeta)>0$ in Eq. (24).

## III. COMPARISON WITH THE KROTOV ITERATIVE METHOD

It can be shown that a simple approximation of $f_\mu(t)$ in Eq. (11),

$$f_\mu(t) \approx g_\mu^{(1)}(t) \equiv -\frac{2}{\hbar}\mathrm{Im}\{\langle\psi^{(0)}(t)|O(t)\mu|\tilde{\psi}(t)\rangle\}, \quad (27)$$

yields the well-known Krotov iterative method [23–25]

$$\tilde{E}(t) = E^{(0)}(t) + \eta S(t) g_\mu^{(1)}(t). \quad (28)$$

Here the Krotov wave function

$$|\tilde{\psi}(t)\rangle = \tilde{U}(t,0)|\psi(0)\rangle \quad (29)$$

evolves according to the time-dependent Schrödinger equation

$$\frac{\partial}{\partial t}|\tilde{\psi}(t)\rangle = \frac{1}{\imath\hbar}\{H_0 - \mu\tilde{E}(t)\}|\tilde{\psi}(t)\rangle, \quad (30)$$

which in turn leads to the equation

$$\frac{\partial}{\partial t}\tilde{U}(t,0) = \frac{1}{\imath\hbar}(H_0 - \mu\tilde{E}(t))\tilde{U}(t,0), \quad \tilde{U}(0,0) = \mathbf{I}. \quad (31)$$

From Eq. (10) and defining $\langle\widetilde{O(t)}\rangle \equiv \langle\tilde{\psi}(t)|O(t)|\tilde{\psi}(t)\rangle$, it is seen that Eq. (28) leads to

$$\frac{d}{dt}\langle\widetilde{O(t)}\rangle = \eta S(t)\tilde{f}_\mu(t)g_\mu^{(1)}(t), \quad (32)$$

where

$$\tilde{f}_\mu(t) \equiv -\frac{2}{\hbar}\mathrm{Im}\{\langle\tilde{\psi}(t)|O(t)\mu|\tilde{\psi}(t)\rangle\}. \quad (33)$$

The rate of change $d\langle\widetilde{O(t)}\rangle/dt$, cf. Eq. (32), may not always be positive (i.e., the Krotov method does not have the LCT characteristic), in contrast to Eq. (22). However, a further manipulation using Eqs. (8), (27), and (28) produces the following relation:

$$\begin{aligned}
\langle\widetilde{O(T)}\rangle - \langle O(0)\rangle &\equiv \langle\tilde{\psi}(t)|O(T)|\tilde{\psi}(T)\rangle - \langle\psi^{(0)}(T)|O(T)\psi^{(0)}(T)\rangle \\
&= \langle\psi^{(0)}(T) + \delta\psi(T)|O(T)|\psi^{(0)}(T) + \delta\psi(T)\rangle - \langle\psi^{(0)}(T)|O(T)|\psi^{(0)}(T)\rangle \\
&= 2\Re\{\langle\psi^{(0)}(T)|O(T)|\delta\psi(T)\rangle\} + \langle\delta\psi(T)|O(T)|\delta\psi(T)\rangle \\
&= \int_0^T \left(-\frac{2}{\hbar}\mathrm{Im}\langle\psi^{(0)}(t)|O(t)\mu|\tilde{\psi}(t)\rangle\right)\{\tilde{E}(t) - E^{(0)}(t)\}dt + \langle\delta\psi(T)|O(T)|\delta\psi(T)\rangle \\
&= \eta\int_0^T S(t)[g_\mu^{(1)}(t)]^2 + \langle\delta\psi(T)|O(T)|\delta\psi(T)\rangle \geq 0,
\end{aligned} \quad (34)$$

which is always positive, thus guaranteeing the monotonicity of the Krotov iterative method based on Eq. (28), as long as the observable $O(T)=O_T$ is positive semidefinite. Here "$\Re$" denotes the real part of a complex number and the following relations were used in the derivations:

$$|\delta\psi(T)\rangle = |\tilde{\psi}(T)\rangle - |\psi^{(0)}(T)\rangle = U_0(T,0)\delta\tilde{U}(T,0)|\psi(0)\rangle, \quad (35)$$

$$\delta\tilde{U}(T,0) = -\frac{1}{\imath\hbar}\int_0^T U_0^\dagger(t,0)\mu\tilde{U}(t,0)\{\tilde{E}(t) - E^{(0)}(t)\}dt. \quad (36)$$

It is in general difficult to quantitatively compare any TBQCP iterative scheme based on Eq. (17) with its Krotov counterpart based on Eq. (28), since there exists no simple relation between the Krotov wave function $|\tilde{\psi}(t)\rangle$ and the exact wave function $|\psi(t)\rangle$. However, in the limit of $\eta\to 0$, we have $\tilde{E}(t)\approx E(t)$, leading to $|\tilde{\psi}(t)\rangle\approx|\psi(t)\rangle$ and $\tilde{f}_\mu(t)$

$\approx f_\mu(t)$. Then, it can be shown, by invoking Eqs. (19), (27), (32), and (34), that

$$\begin{aligned}\langle O(T)\rangle - \langle \widetilde{O(T)}\rangle &= \eta\int_0^T S(t)[f_\mu(t)]^2 dt - \int_0^T \frac{d}{dt}\langle \widetilde{O(t)}\rangle \\ &\approx \eta\int_0^T S(t)\{[\tilde{f}_\mu(t)]^2 - \tilde{f}_\mu(t) g_\mu^{(1)}(t)\}dt \\ &= \eta\int_0^T S(t)\left[-\frac{2}{\hbar}\mathrm{Im}\langle \delta\psi(t)|O(t)\mu|\tilde{\psi}(t)\rangle\right]^2 dt \\ &\quad + \langle \delta\psi(T)|O(T)|\delta\psi(T)\rangle \geq 0, \end{aligned} \tag{37}$$

which implies that the TBQCP method based on Eq. (17) may have a numerical advantage over the Krotov method based on Eq. (28) when the parameter $\eta$ is sufficiently small, since $\langle \widetilde{O(T)}\rangle$ may be considered as a lower bound of $\langle O(T)\rangle$.

## IV. RELATIONSHIP WITH VARIATIONAL OCT

The OCT equations (the first-order necessary optimality conditions) are commonly derived upon the variation of a cost functional [2–6,25]

$$\begin{aligned} J[\psi,\lambda,E] &= \langle\psi(T)|O|\psi(T)\rangle - \int_0^T \frac{\alpha}{S(t)}[E(t)-E^{(0)}(t)]^2 dt \\ &\quad + \left\{\int_0^T \left\langle \lambda(t)\left|\left[\frac{1}{\iota\hbar}(H_0-\mu E(t)) - \frac{\partial}{\partial t}\right]\right|\psi(t)\right\rangle dt \right. \\ &\quad \left. + \text{c.c.}\right\}, \end{aligned} \tag{38}$$

where $|\lambda(t)\rangle$ is the corresponding Lagrange multiplier. The penalty term with $\alpha>0$ in Eq. (38) seeks to minimize either the difference of the optimal control field and its reference control field $E^{(0)}(t)$ or the fluence of the control field with the commonly adopted zero reference control field $E^{(0)}(t)=0$. The resultant first-order OCT conditions, in addition to Eq. (1), are

$$\frac{\partial}{\partial t}|\lambda(t)\rangle = \frac{1}{\iota\hbar}\{H_0-\mu E(t)\}|\lambda(t)\rangle, \tag{39}$$

subject to the boundary condition $|\lambda(T)\rangle = O_T|\psi(T)\rangle$, and

$$E(t) = E^{(0)}(t) + \frac{1}{2\alpha}S(t)g_\mu(t), \tag{40}$$

where the gradient $g_\mu(t)$ is

$$\begin{aligned} g_\mu(t) &\equiv \frac{\delta\langle\psi(T)|O_T|\psi(T)\rangle}{\delta E(t)} \\ &= -\frac{2}{\hbar}\mathrm{Im}\{\langle\lambda(t)|\mu|\psi(t)\rangle\} \\ &= -\frac{2}{\hbar}\mathrm{Im}\{\langle\psi(t)|[U(t,T)O_T U(T,t)]\mu|\psi(t)\rangle\}, \end{aligned} \tag{41}$$

which may be compared with $f_\mu(t)$ in Eq. (11). It is readily found that upon $E^{(0)}(t)$ approaching an optimal solution, then $U_0(t,T)\to U(t,T)$ and $f_\mu(t)\to g_\mu(t)$. Consequently, the TBQCP Eqs. (11) and (21), respectively, lead to OCT Eqs. (41) and (40), indicating that the time-dependent operator $O(t)\equiv U(t,T)O_T U^\dagger(t,T)$ associated with an optimal control field is necessarily a dynamical invariant, i.e.,

$$\frac{\partial}{\partial t}O(t) = \frac{1}{\iota\hbar}[H_0-\mu E(t), O(t)], \quad O(T)=O_T, \tag{42}$$

such that $(\partial/\partial t)(O(t)|\psi(t)\rangle) = (1/\iota\hbar)\{H_0-\mu E(t)\}(O(t)|\psi(t)\rangle)$ and $(d/dt)\langle\psi(t)|O(t)|\psi(t)\rangle = 0$ [39]. Equations (39) and (42) are equivalent and can be exploited for efficient numerical implementation. In principle, Eqs. (1), (42), and (40) need to be solved iteratively, via forward-backward propagations starting with the initial condition $|\psi(0)\rangle$ and the reference field $E^{(0)}(t)$. Computationally, various numerical schemes can be adopted for practical implementation of the underlying iterative procedures. For example, the substitution of $E(t)$ by $E^{(0)}(t)$ in Eq. (42) yields the relations $O(t) = U_0(t,T)O_T U_0^\dagger(t,T)$ and $g_\mu(t)=f_\mu(t)$, which immediately lead to TBQCP in Eq. (21).

## V. ACCELERATED MONOTONICALLY CONVERGENT TBQCP SCHEMES

To implement efficient and robust monotonically convergent schemes based on TBQCP, we recast Eqs. (11), (17), and (18) into the following recurrence relation:

$$\begin{aligned} E^{(n+1)}(t) &= E^{(n)}(t) + (1-\zeta^{(n+1)})\eta S(t) f_\mu^{(n+1)}(t) \\ &\quad + \eta S(t) f^{(n+1)}(t), \quad n=0,1,\ldots, \end{aligned} \tag{43}$$

where

$$f_\mu^{(n+1)}(t) \equiv -\frac{2}{\hbar}\mathrm{Im}\{\langle\psi^{(n+1)}(t)|O^{(n)}(t)\mu|\psi^{(n+1)}(t)\rangle\} \tag{44}$$

and

$$\zeta^{(n+1)} \equiv \frac{\int_0^T S(t) f_\mu^{(n+1)}(t) f^{(n+1)}(t)dt}{\int_0^T S(t)[f_\mu^{(n+1)}(t)]^2 dt} \approx \frac{\int_0^T S(t) f_\mu^{(n)}(t) f^{(n+1)}(t)dt}{\int_0^T S(t)[f_\mu^{(n)}(t)]^2 dt}. \tag{45}$$

Here $\eta>0$ denotes the iteration step parameter, $(1-\zeta^{(n+1)})$ is the acceleration parameter, and $f^{(n+1)}(t)$ is a free function that can be chosen as either zero or a nonzero function of time $t$. Moreover,

$$\frac{\partial}{\partial t}O^{(n)}(t) = -\frac{1}{\iota\hbar}[O^{(n)}(t), H_0-\mu E^{(n)}(t)], \quad O(T)=O_T \tag{46}$$

and

$$\frac{\partial}{\partial t}|\psi^{(n+1)}(t)\rangle = \frac{1}{\iota\hbar}\{H_0-\mu E^{(n+1)}(t)\}|\psi^{(n+1)}(t)\rangle,$$

$$|\psi^{(n+1)}(0)\rangle = |\psi^{(0)}(0)\rangle. \quad (47)$$

From Eq. (20), it can be shown that the expectation value $\langle O^{(n)}(t)\rangle$ increases from iteration to iteration:

$$\langle O^{(0)}(0)\rangle \to \langle O^{(0)}(T)\rangle = \langle O^{(1)}(0)\rangle \to \langle O^{(1)}(T)\rangle \cdots \langle O^{(n)}(0)\rangle \to \langle O^{(n)}(T)\rangle = \langle O^{(n+1)}(0)\rangle \to \langle O^{(n+1)}(T)\rangle \cdots . \quad (48)$$

The following material presents three numerically expedient schemes for implementation of Eq. (43). The first scheme corresponds to the zero free function $f^{(n+1)}(t)=0$ for all $n=0,1,2,\ldots$. The second and third schemes are chosen for nonzero free functions $f^{(n+1)}(t)\neq 0$ to make the acceleration parameter $(1-\zeta^{(n+1)})$ as large as possible throughout the iterations, cf. Eq. (25). To avoid the expensive computation of the integrals in Eq. (45) that gives rise to the parameter $\zeta^{(n+1)}$, these two latter schemes are formulated based on the behavior of the parameter $\zeta^{(n+1)}$ in the limit of a sufficiently small $\eta$ (i.e., $\eta\to 0$) [or of a sufficiently large $n$ (i.e., $n\gg 1$)].

*Scheme (i)*: $f^{(n+1)}(t)=0\ \forall n\geq 0$, $\eta\neq 0$, and $\zeta^{(n+1)}=0$: Here Eq. (43) reduces to the monotonic convergence algorithm of Mirrahimi, Turinici, and Rouchon [17]:

$$E^{(n+1)}(t) = E^{(n)}(t) + \eta S(t) f_\mu^{(n+1)}(t) \quad \text{(TBQCP-1)}, \quad (49)$$

for $n=0,1,\ldots$, in agreement with Eq. (23). This scheme advances the control field from $E^{(n)}(t)$ to $E^{(n+1)}(t)$, with an iteration step parameter equal to $\eta$, along with the evolution of the wave function $|\psi^{(n+1)}(t)\rangle$ from its initial one $|\psi^{(0)}(0)\rangle$, cf. Eq. (47).

*Scheme (ii)*: $f^{(1)}(t)=0$ and $\eta S(t) f^{(n+1)}(t) = -a\{E^{(n)}(t) - E^{(n-1)}(t)\}$, $0<a\leq 1$, for $n\geq 1$. Here Eq. (43) becomes

$$\begin{cases} E^{(1)}(t) = E^{(0)}(t) + \eta S(t) f_\mu^{(1)}(t) \\ E^{(n+1)}(t) = (1-a)E^{(n)}(t) + aE^{(n-1)}(t) \\ \qquad + (1-\zeta^{(n+1)})\eta S(t) f_\mu^{(n+1)}(t), \\ \qquad \text{for } n = 1,2,\ldots, \end{cases} \quad \text{(TBQCP-2n)}, \quad (50)$$

where

$$\zeta^{(n+1)} = -\frac{a}{\eta}\frac{\int_0^T f_\mu^{(n+1)}(t)(E^{(n)}(t) - E^{(n-1)}(t))dt}{\int_0^T S(t)[f_\mu^{(n+1)}(t)]^2 dt} \approx -\frac{a}{\eta}\frac{\int_0^T f_\mu^{(n)}(t)(E^{(n)}(t) - E^{(n-1)}(t))dt}{\int_0^T S(t)[f_\mu^{(n)}(t)]^2 dt}. \quad (51)$$

For a sufficiently small $\eta$ (as well as for a sufficiently large $n$), $E^{(n+1)}(t)-E^{(n)}(t)\approx E^{(n)}(t)-E^{(n-1)}(t)$, thus leading to $\zeta^{(n+1)}\approx -a<0$, after invoking Eqs. (50) and (51). By choosing $f^{(1)}(t)=0$ and $\zeta^{(n+1)}=-a\ \forall n\geq 1$, Eq. (50) may be simplified as

$$\begin{cases} E^{(1)}(t) = E^{(0)}(t) + \eta S(t) f_\mu^{(1)}(t) \\ E^{(n+1)}(t) = (1-a)E^{(n)}(t) + aE^{(n-1)}(t) \\ \qquad + (1+a)\eta S(t) f_\mu^{(n+1)}(t), \\ \qquad \text{for } n = 1,2,\ldots \end{cases} \quad \text{(TBQCP-2)}, \quad (52)$$

The value of the parameter $a$ in Eq. (52) is chosen to lie between 0 and 1 to prevent the factor $(1-a)$ from becoming a negative number, which would result in a undesired subtraction of the current control field $E^{(n)}(t)$. Of special interest in this scheme are the two cases: (1) $a=1$ and (2) $a=0.5$, which lead, respectively, to two distinct iterative steps:

$$E^{(n+1)}(t) = E^{(n-1)}(t) + 2\eta S(t) f_\mu^{(n+1)}(t), \quad n\geq 1, \quad (53)$$

and

$$E^{(n+1)}(t) = \frac{1}{2}(E^{(n)}(t) + E^{(n-1)}(t)) + \frac{3}{2}\eta S(t) f_\mu^{(n+1)}(t), \quad n\geq 1. \quad (54)$$

The former, Eq. (53), advances the control field from $E^{(n-1)}(t)$ to $E^{(n+1)}(t)$ with an iteration step size equal to $2\eta$, while the latter, Eq. (54), advances from the midpoint of $E^{(n)}(t)$ and $E^{(n-1)}(t)$ to $E^{(n+1)}(t)$ with a step size equal to $1.5\eta$, compared to the step size $\eta$ in the TBQCP-1 scheme, Eq. (49). A larger step size allowed in the TBQCP-2 scheme may result in better convergence behavior.

*Scheme (iii)*: $f^{(1)}(t)=0$ and $f^{(n+1)}(t)=-bf_\mu^{(n)}(t)$, $b>0$, for $n\geq 1$. Here we have

$$\begin{cases} E^{(1)}(t) = E^{(0)}(t) + \eta S(t) f_\mu^{(1)}(t) \\ E^{(n+1)}(t) = E^{(n)}(t) - b\eta S(t) f_\mu^{(n)}(t) \\ \qquad + (1-\zeta^{(n+1)})\eta S(t) f_\mu^{(n+1)}(t), \\ \qquad \text{for } n = 1,2,\ldots, \end{cases} \quad \text{(TBQCP-3n)}, \quad (55)$$

where $\zeta^{(2)}=-b$ and

$$\zeta^{(n+1)} = -b\frac{\int_0^T S(t) f_\mu^{(n+1)}(t) f_\mu^{(n)}(t)dt}{\int_0^T S(t)[f_\mu^{(n+1)}(t)]^2 dt} \approx -b\frac{\int_0^T S(t) f_\mu^{(n)}(t) f_\mu^{(n-1)}(t)dt}{\int_0^T S(t)[f_\mu^{(n)}(t)]^2 dt}, \quad n\geq 2. \quad (56)$$

For a sufficiently small $\eta$ (as well as for a sufficiently large $n$), $f_\mu^{(n)}(t)$ changes only gradually, i.e., $f_\mu^{(n)}(t)\approx f_\mu^{(n+1)}(t)$, thus, from Eq. (56), we obtain $\zeta^{(n+1)}\approx -b$. By adopting $f^{(1)}(t)=0$ and $\zeta^{(n+1)}=-b\ \forall n\geq 1$, Eq. (55) may be cast as

$$\begin{cases} E^{(1)}(t) = E^{(0)}(t) + \eta S(t) f_\mu^{(1)}(t) \\ E^{(n+1)}(t) = E^{(n)}(t) - b\,\eta S(t) f_\mu^{(n)}(t) \quad \text{(TBQCP-3)}, \\ \qquad + (1+b)\,\eta S(t) f_\mu^{(n+1)}(t), \\ \qquad \text{for } n = 1,2,\ldots. \end{cases} \tag{57}$$

It is instructive to note that $E^{(n+1)}(t)$ in Eq. (57) can be succinctly cast as

$$E^{(n+1)}(t) = \bar{E}^{(n)}(t) + (1+b)\,\eta S(t) f_\mu^{(n+1)}(t), \quad n \geq 0, \tag{58}$$

where

$$\begin{aligned} \bar{E}^{(n)}(t) &= \beta E^{(n)}(t) + (1-\beta)\bar{E}^{(n-1)}(t) \\ &= \beta \sum_{k=0}^{n-2} (1-\beta)^k E^{(n-k)}(t) + (1-\beta)^{n-1}\bar{E}^{(0)}(t) \end{aligned} \tag{59}$$

with $0 < \beta \equiv 1/(1+b) < 1.0$ and $\bar{E}^{(0)}(t) \equiv \{(1-b)E^{(1)}(t) + bE^{(0)}(t)\}$. Here $\bar{E}^{(n)}(t)$ is the exponentially weighted (geometric) moving average (EWMA) [45–48] of the $(n+1)$ control fields $E^{(n)}(t), E^{(n-1)}(t), \ldots, E^{(2)}(t), E^{(1)}(t), E^{(0)}(t)$ generated at the current and all past iterations [including the initial reference control field $E^{(0)}(t)$], with exponentially decreasing weights $1, 1-\beta, (1-\beta)^2, \ldots, (1-\beta)^{(n-2)}, (1-\beta)^{(n-1)}$ and $(1-\beta)^{n-1}$, respectively. Of special interest is the case of $b=1$ which results in

$$\begin{aligned} E^{(n+1)}(t) = \frac{1}{2}\Bigg( E^{(n)}(t) + \frac{1}{2}\Bigg( E^{(n-1)}(t) + \cdots \\ + \frac{1}{2}\Bigg\{ E^{(2)}(t) + \frac{1}{2}[E^{(1)}(t) + E^{(0)}(t)] \Bigg\} \cdots \Bigg) \Bigg) \\ + 2\,\eta S(t) f_\mu^{(n+1)}(t), \end{aligned} \tag{60}$$

showing that the control field is being advanced from the corresponding EWMA of the current and past control fields with an exponential weighting factor equal to 1/2 and with an iteration step size equal to $2\eta$.

There are several relevant observations regarding the three TBQCP schemes given in Eqs. (49), (52), and (57): First, (1) in the limit of $a \to 0$ and $b \to 0$, the schemes TBQCP-2 and TBQCP-3 reduce to the scheme TBQCP-1. (2) In general, all three schemes start off at the same pace, i.e., $E^{(1)}(t) = E^{(0)}(t) + \eta S(t) f_\mu^{(1)}(t)$, however, they behave differently after the second iteration. For example, the second step can be written as

$$\begin{cases} E^{(2)}(t) = E^{(1)}(t) + \eta S(t) f_\mu^{(2)}(t), & \text{(TBQCP-1)}, \\ E^{(2)}(t) = E^{(0)}(t) + 2\,\eta S(t) f_\mu^{(2)}(t), & \text{(TBQCP-2)}, \\ E^{(2)}(t) = \frac{1}{2}[E^{(1)}(t) + E^{(0)}(t)] + 2\,\eta S(t) f_\mu^{(2)}(t), & \text{(TBQCP-3)} \end{cases} \tag{61}$$

in the case of $a=b=1.0$, and

$$\begin{cases} E^{(2)}(t) = E^{(1)}(t) + \eta S(t) f_\mu^{(2)}(t), & \text{(TBQCP-1)}, \\ E^{(2)}(t) = \frac{1}{2}[E^{(1)}(t) + E^{(0)}(t)] + \frac{3}{2}\eta S(t) f_\mu^{(2)}(t), & \text{(TBQCP-2)}, \\ E^{(2)}(t) = \frac{1}{2}[E^{(1)}(t) + E^{(0)}(t)] + 2\,\eta S(t) f_\mu^{(2)}(t) & \text{(TBQCP-3)} \end{cases} \tag{62}$$

in the case of $a=0.5$ and $b=1.0$. These two special cases clearly display the advantage of TBQCP-3 and TBQCP-2 over TBQCP-1. Finally, (3) the parameter $b$ of TBQCP-3, cf. Equation (57), may be chosen to be as large as possible for maximize the convergence as long as it does not cause numerical instability. Especially, in the limit of $b \gg 1$, i.e., $\beta \approx 0$, Eq. (58) reduces to

$$\begin{aligned} E^{(n+1)}(t) \approx (1-b)E^{(1)}(t) + bE^{(0)}(t) \\ + (1+b)\,\eta S(t) f_\mu^{(n+1)}(t), \quad n \geq 1, \ b \gg 1, \end{aligned} \tag{63}$$

corresponding to a rather large iterative step size of $(1+b)\,\eta \sim b\,\eta \gg 1$.

Moreover, the parameters $\eta > 0$, $0 < a \leq 1$, and $b > 0$ may all be optimized throughout the iterations to maximize the convergence, for example, by exerting some adaptive control over these parameters. Only the scheme TBQCP-1 assures monotonicity over time, cf. Eq. (22). Although, in principle, the monotonicity of TBQCP-2 and TBQCP-3 holds strictly in the limit of $\eta \to 0$ (as well as in the limits of $n \gg 1$), in practice, it may still hold for finite $\eta$ and $n$ values. The extent that both TBQCP-2 and TBQCP-3 iterative schemes behave monotonically is examined numerically in Sec. VI. The convergence behavior of the three TBQCP-based iteration schemes proposed in Eqs. (49), (52), and (57), as well as that of the Krotov algorithm in Eq. (28), will be illustrated in Sec. VI for optimal control simulations on a model quantum system. To facilitate the implementation of efficient and robust TBQCP iterative schemes, a numerical procedure for solving Eq. (46) and computing $f_\mu^{(n+1)}(t)$ in Eq. (44) is described in Appendix A.

## VI. ILLUSTRATIONS

The aim of this section is to assess and demonstrate the capability of the TBQCP-based schemes using a prototypical quantum control problem. Specifically, we consider control of state-to-state vibrational transitions based on a model of the OH diatom in the ground electronic state. The one-dimensional (1D) potential energy of the OH is expressed as a Morse oscillator [27]

$$V(r) = D_e\{1 - \exp[-\kappa(r - r_e)]\}^2 - D_e, \tag{64}$$

where $D_e = 0.1994$ a.u., $r_e = 1.821$ a.u., and $r$ are, respectively, the corresponding dissociation energy, the equilibrium bound length, and the internuclear distance, and $\kappa = 1.189$ a.u.. The OH model potential has 22 bound levels and a well depth of approximately 0.2 a.u., corresponding to a characteristic time of $\Delta\tau = 2\pi/0.2$ a.u. $\approx 31.4$ a.u.. The di-

pole moment function $\mu(r)$ of OH has form [27]

$$\mu(r) = 3.088r \exp\left(-\frac{r}{0.6}\right) \quad \text{(in a.u.)}. \tag{65}$$

The calculations are performed with 512 evenly spaced discretized grid points over the OH internuclear distance $0.0 \leq r \leq 15.0$ a.u. (i.e., $r_{\max}=15$ a.u.). The model OH dipole moment matrix elements between the immediate adjacent bound levels range from 0.0371 a.u. for the $0 \rightarrow 1$ transition, to 0.0788 a.u. (i.e., the largest value) for the $8 \rightarrow 9$ transition, and finally to 0.010 a.u. (i.e., the smallest value) for the $20 \rightarrow 21$ transition. In general, the transition dipole moment between any two bound levels $\nu$ and $\nu'$ decreases rapidly as the difference $\Delta\nu=|\nu-\nu'|$ increases. For example, the transition dipole moments are $6.882\times10^{-3}$ a.u., $1.051\times10^{-4}$ a.u., $4.238\times10^{-7}$ a.u., $1.17\times10^{-7}$ a.u., and $1.829\times10^{-8}$ a.u., respectively, for the $0\rightarrow2$, $0\rightarrow5$, $0\rightarrow9$, $0\rightarrow15$, and $0\rightarrow21$ transitions. As a result of these rapidly decreasing transition dipole moments, it is more difficult to obtain an optimal control field for maximizing the transition probability between two disparate levels than between adjacent or nearby levels.

To show the utility of various TBQCP based monotonically convergent algorithms, in the following numerical simulations we will consider the control of the transition probability for the two far separated vibrational levels $\nu=0$ and $\nu'=15$. These calculations will be compared with those using the Krotov method. The target observable $O(T)$ in the following simulations is taken to be the projection operator

$$O(T) = |\nu'\rangle\langle\nu'|, \tag{66}$$

corresponding to the target state $\nu'$. The resultant expectation value of the corresponding dynamical invariant $O(t)$ can then be expressed as

$$\langle O^{(n)}(t)\rangle = \langle\psi^{(n+1)}(t)|\varphi^{(n)}_{\nu'}(t)\rangle\langle\varphi^{(n)}_{\nu'}(t)|\psi^{(n+1)}(t)\rangle \geq 0, \tag{67}$$

and Eq. (44) reduces to

$$f^{(n+1)}_{\mu}(t) = -\frac{2}{\hbar}\mathrm{Im}\langle\psi^{(n+1)}(t)|\varphi^{(n)}_{\nu'}(t)\rangle\langle\varphi^{(n)}_{\nu'}(t)|\mu|\psi^{(n+1)}(t)\rangle, \tag{68}$$

where

$$\frac{\partial}{\partial t}|\varphi^{(n)}_{\nu'}(t)\rangle = \frac{1}{\imath\hbar}\{H_0 - \mu E^{(n)}(t)\}|\varphi^{(n)}_{\nu'}(t)\rangle, \quad |\varphi^{(n)}_{\nu'}(T)\rangle = |\nu'\rangle. \tag{69}$$

It is expected that $|\psi^{(n+1)}_{\nu'}(t)\rangle \rightarrow |\varphi^{(n)}(t)\rangle$, $f^{(n+1)}_{\mu}(t) \rightarrow 0$, and $\langle O(T)\rangle \rightarrow 1$ in the limit of a sufficiently large number of iterations ($n \gg 1$). The function $f^{(n+1)}_{\mu}(t)$ in Eq. (68) at the $(n+1)$th iteration, expressed in terms of the quantities $\langle\psi^{(n+1)}(t)|\varphi^{(n)}_{\nu'}(t)\rangle$ and $\langle\varphi^{(n)}_{\nu'}(t)|\mu|\psi^{(n+1)}(t)\rangle$, can be computed from (i) the time-dependent dynamical invariant eigenstate $\langle r|\varphi^{(n)}_{\nu'}(t)\rangle$ (as a function of the internuclear distance $r$) and (ii) the time-dependent wave function $\langle r|\psi^{(n+1)}(t)\rangle$ corresponding to the boundary conditions $\langle r|\varphi^{(n)}_{\nu'}(T)\rangle=\langle r|\nu'\rangle$ and $\langle r|\psi^{(n+1)}(0)\rangle=\langle r|\nu\rangle$. The control field $E^{(n+1)}(t)$ is then evaluated iteratively using various TBQCP-based updating schemes described in Sec. V. These operations are set out in Appendix B.

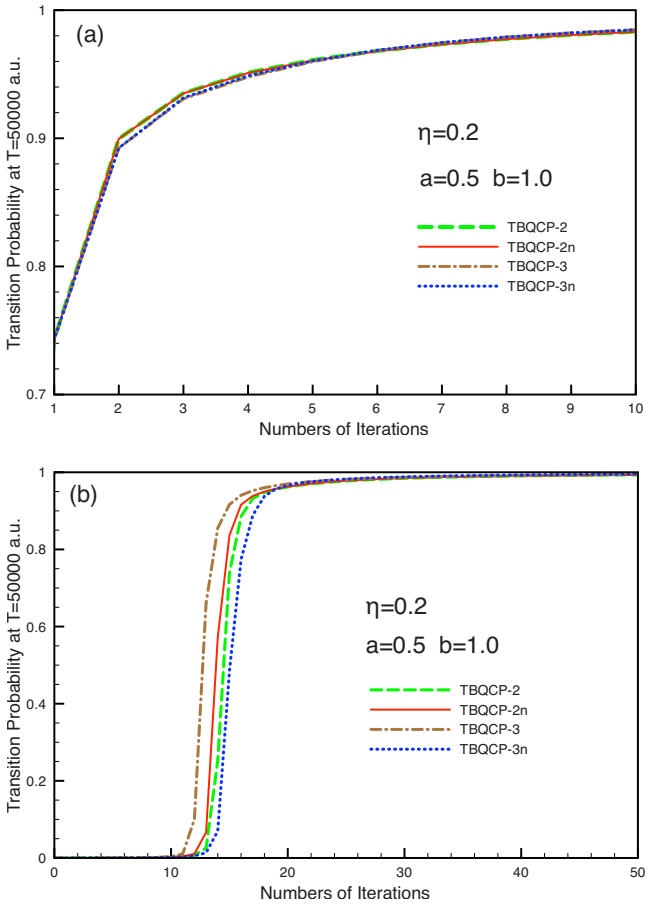


FIG. 1. (Color online) (Color online) The transition probability $P_{0\rightarrow15}(T)$ for $T=50\,000$ a.u.($\sim$1.21 ps), as a function of iteration, for the schemes TBQCP-2, TBQCP-2n, TBQCP-3, and TBQCP-3n schemes [Eqs. (52), (50), (57), and (55)] for the parameters $\eta=0.2$, $a=0.5$, and $b=1.0$: (a) $A=8.8$ a.u., corresponding to an initial transition probability of $P_{0\rightarrow15}(T)=0.121$, and (b) $A=8.0$ a.u., corresponding to an initial transition probability of $P_{0\rightarrow15}(T)=0.000\,11$, based on the LCT generated initial control fields. In panel (a), the dashed (TBQUCP-2) and solid (TBQCP-2n) curves are indistinguishable, the dash-dotted (TBQCP-3) and dotted (TBQCP-3n) curves are indistinguishable.

Furthermore, we have considered two different initial control fields in the simulations in order to assess the convergence properties of the TBQCP schemes in comparison with the Krotov method. The calculations in Figs. 1–4 were based on the LCT generated initial control fields and Figs. 5–7 used negative linearly chirped initial control fields. Specifically, the LCT initial control fields were generated using the relation

$$E^{(0)}(t) = S(t)\left\{-\frac{2}{\hbar}\mathrm{Im}[\langle\psi^{(0)}(t)|O_{\mathrm{LCT}}\mu|\psi^{(0)}(t)\rangle]\right\} \tag{70}$$

and the negative linearly chirped initial control fields were computed using the expression

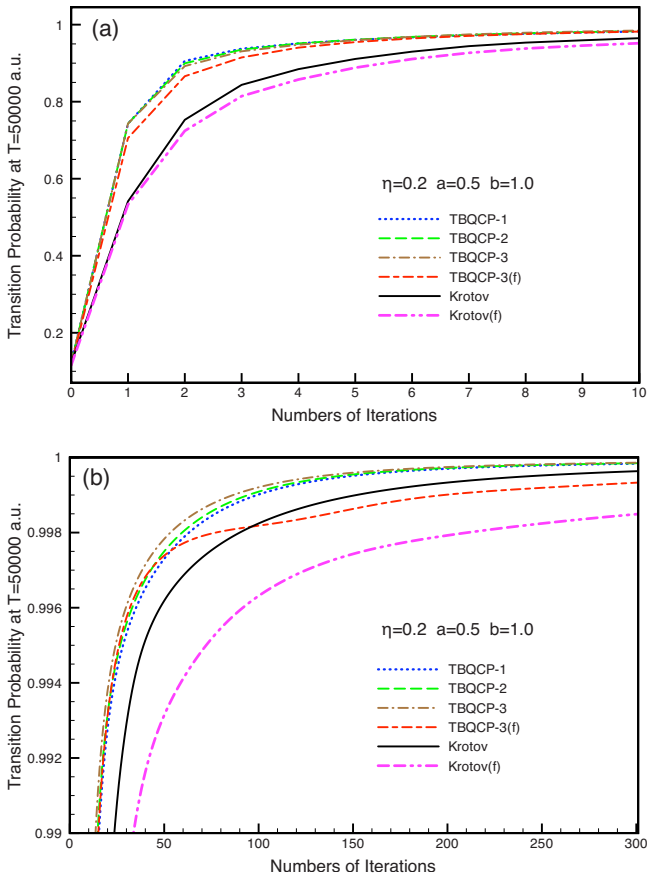


FIG. 2. (Color online) The transition probability $P_{0\to 15}(T)$ for $T=50\,000$ a.u.($\sim 1.21$ ps), as a function of iteration, for different TBQCP schemes ($a=0.5$, and $b=1.0$) and the Krotov method for the parameters $\eta=0.2$: (a) first 10 iterations and (b) iterations near the maximum yield (15–300). The initial transition probability is $P_{0\to 15}(T)=0.121$, corresponding to a LCT generated initial control field with $A=8.8$ a.u. The filter frequency window is [0.005, 0.05] in atomic units.

$$E^{(0)}(t) = S(t)\cos\left[\left(1.2 - \frac{t}{2T}\right)\omega_{10}t\right], \tag{71}$$

where $O_{\mathrm{LCT}}[\equiv\Sigma_{k=\nu}^{\nu'}(k-\nu)|k\rangle\langle k|/(\nu'-\nu)]$ commutes with the field-free Hamiltonian $H_0$, $S(t)$ $[=A\ \sin^2\ \pi t/T, A>0]$ denotes the pulse shape, and $\omega_{10}(=0.01724$ a.u.) is the transition frequency between the ground and first excited vibrational levels of the 1D OH model diatom. The transition frequency between the 14th and 15th vibrational levels is 0.00579 a.u. and that between the ground vibrational level and the 15th vibrational level is 0.17276 a.u., compared to a width of $\sim 0.0044$ a.u. at the half-maximum and a frequency of $\sim 0.0119$ a.u. at the maximum of the negative chirped field given in Eq. (71). The initial negative linearly chirped field in Eq. (71) was adopted to explore the convergence behavior of the TBQCP schemes over a wide range of different values of $\eta$ (for all TBQCP schemes, as well as the Krotov method) and $b$ (for TBQCP-3). In the following simulations, we consider two different pulse lengths $T=50\,000$ a.u.($\sim 1.21$ ps), for both the LCT generated initial control fields and the

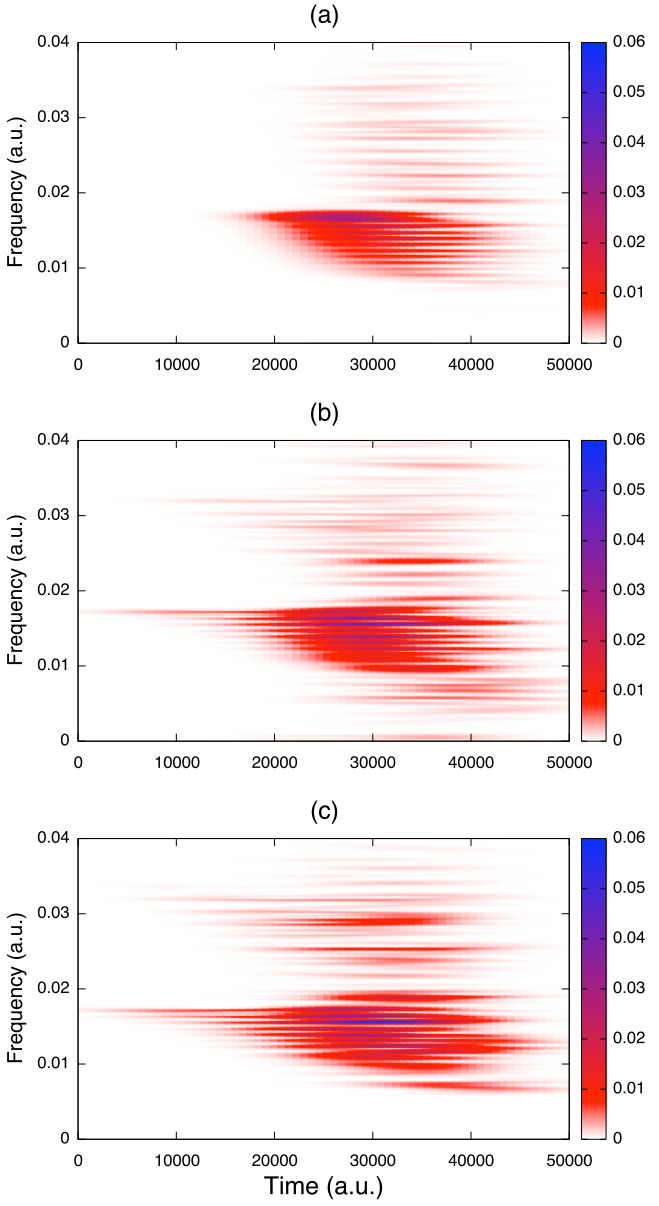


FIG. 3. (Color online) The windowed Fourier transform (WFT) power spectra, as a function of the propagation time and frequency, for the initial LCT and final TBQCP-3 ($\eta=0.2$, $b=1.0$) control fields for $T=50\,000$ a.u.($\sim 1.21$ ps): (a) LCT initial control field WFT power spectrum ($A=8.8$ a.u.), (b) unfiltered TBQCP-3 control field WFT power spectrum, (c) filtered TBQCP-3 control field WFT power spectrum. The time-window width for the WFT is 6250 a.u. ($\sim 0.15$ ps).

negative linearly chirped initial control fields, and $T=10\,000$ a.u.($\sim 0.24$ ps), for the negative linearly chirped initial control fields. In both cases, the time interval $[0,T]$ is divided into $2^{15}=32768$ evenly divided subintervals for numerical integration of the corresponding time-dependent Schrödinger equation, cf. Appendix B. The time integration step size $\Delta t$ is $\Delta t\approx 1.5$ a.u. for $T=50\,000$ a.u. and $\Delta t\approx 0.3$ a.u. for $T=10\,000$ a.u., compared to $\Delta\tau\approx 31.4$ a.u., which is the characteristic time of the 1D OH model diatom, cf. Equations (64) and (65). We remark that it is in general difficult to use the LCT scheme for generating a viable short

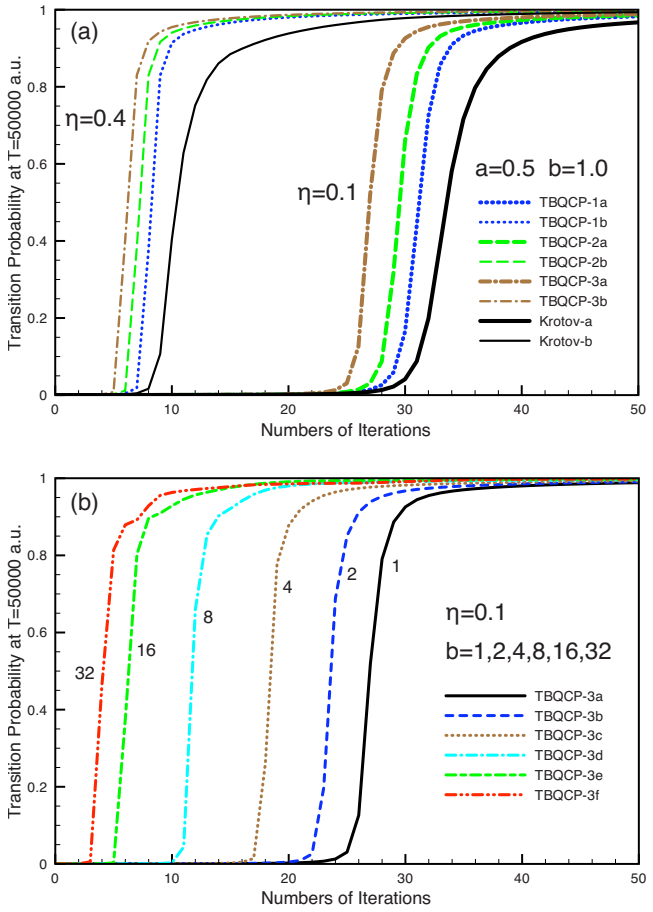


FIG. 4. (Color online) The transition probability $P_{0\to 15}(T)$ for $T=50\,000$ a.u.($\sim 1.21$ ps) as a function of iteration. (a) Different TBQCP schemes ($a=0.5$, $b=1.0$) and the Krotov method for different $\eta$: $\eta=0.1$ (thick curves) for TBQCP-1a,TBQCP-2a,TBQCP-3a, and Krotov-a and $\eta=0.4$ (thin curves) for TBQCP-1b,TBQCP-2b,TBQCP-3b, and Krotov-b; and (b) the TBQCP-3 scheme ($\eta=0.1$) for different $b$: 1.0 (TBQCP-3a), 2.0 (TBQCP-3b), 4.0 (TBQCP-3c), 8.0 (TBQCP-3d), 16.0 (TBQCP-3e), and 32.0 (TBQCP-3f). The initial control field is generated by the LCT method with $A=8.0$ a.u.

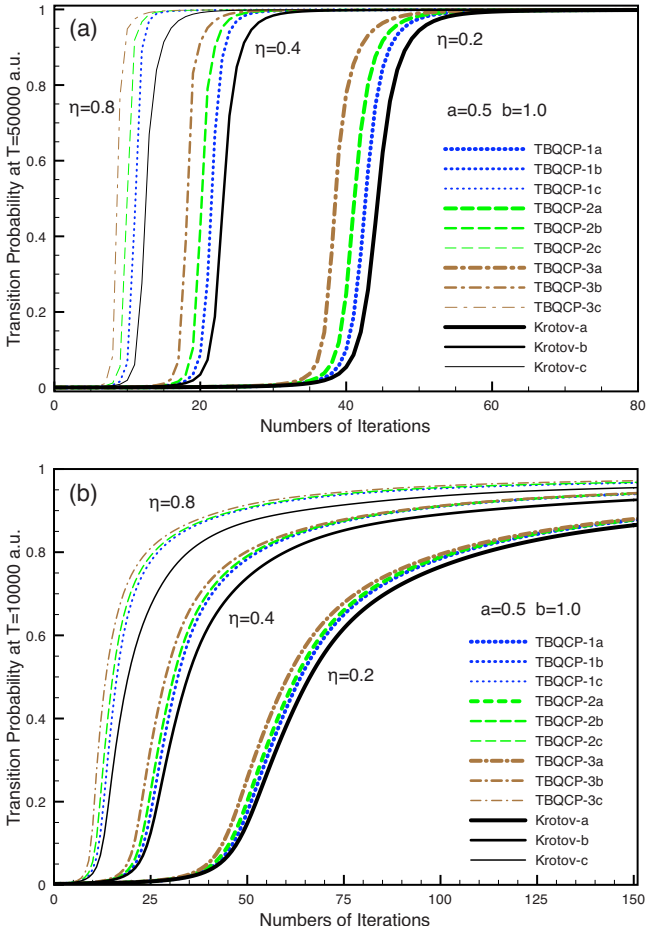


FIG. 5. (Color online) The transition probability $P_{0\to 15}(T)$ for (a) $T=50\,000$ a.u.($\sim 1.21$ ps) and (b) $T=10\,000$ a.u.($\sim 0.24$ ps), as a function of iteration for different TBQCP schemes ($a=0.5$, $b=1.0$) and the Krotov method for different $\eta$: $\eta=0.2$ (thick curves) for TBQCP-1a,TBQCP-2a,TBQCP-3a and Krotov-a; $\eta=0.4$ for TBQCP-1b,TBQCP-2b,TBQCP-3b, and Krotov-b; and $\eta=0.8$ (thin curves) for TBQCP-1c,TBQCP-2c,TBQCP-3c, and Krotov-c. The amplitude of the initial negative linearly chirped control fields: (a) $A=0.015$ a.u. and (b) $A=0.06$ a.u.

initial control field (for example, $T=10\,000$ a.u. in the current study) that yields even a very small transition probability between two disparate vibrational levels (here $\nu=0$ to $\nu'=15$), due to the rather restrictive long temporal characteristics of the LCT method [17]. The control field may also be filtered to remove its DC and high-frequency components. For example, the time-dependent laser field $E(t)$ may be filtered *post facto* at the end of each iteration according to the relation

$$\mathcal{F}^{-1}[\mathcal{F}[E^{(n)}(t)]h(\omega)] \to E^{(n)}(t), \quad n \geq 0, \tag{72}$$

where $\mathcal{F}$ and $\mathcal{F}^{-1}$ are, respectively, Fourier and inverse Fourier transforms and the filter function $h(\omega)$ is chosen (in this work) as the Butterworth band pass filter [49]

$$h(\omega) = \left\{ \left[ 1 + \left( \frac{\omega_\ell}{\omega} \right)^{2m} \right] \left[ 1 + \left( \frac{\omega}{\omega_h} \right)^{2m} \right] \right\}^{-1/2}, \tag{73}$$

with $\omega_\ell$ and $\omega_h$ being the low and high cutoff frequencies, respectively.

Figures 1(a) and 1(b) compare the iterative schemes TBQCP-2 and TBQCP-3 [Eqs. (52) and (57)] with their respective, more expensive counterparts TBQCP-2n and TBQCP-3n [Eqs. (50) and (55)]. Here we have considered two different LCT generated initial control fields described in Eq. (70): (a) $A=8.8$ a.u. in Figs. 1(a) and 1(b) $A=8.0$ a.u. in Fig. 1(b), respectively. Furthermore, the parameters $\eta=0.2$, $a=0.5$, and $b=1.0$ were adopted for the corresponding TBQCP schemes. The integrals involved in Eqs. (51) and (56), for computing the parameter $\zeta^{(n+1)}$, $n=1,2,\ldots$, were carried out using the extended Trapezoidal rule [50] on $2^{15}+1=32769$ evenly spaced grids over the time interval $[0,50\,000$ a.u.$]$. It was found in Fig. 1(a) that the

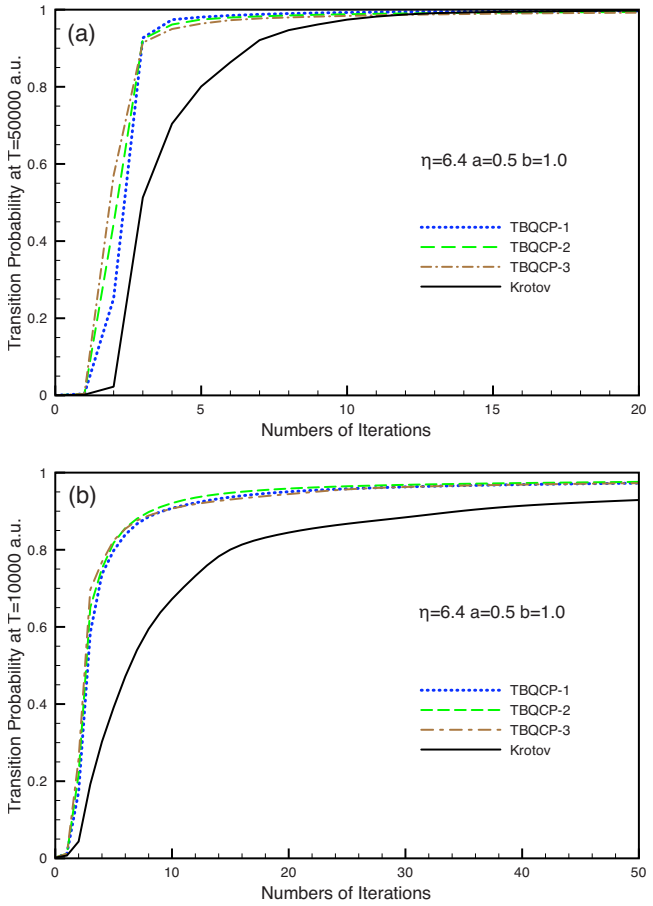


FIG. 6. (Color online) The transition probability $P_{0\to 15}(T)$ for (a) $T=50\,000$ a.u.($\sim 1.21$ ps) and (b) $T=10\,000$ a.u.($\sim 0.24$ ps), as a function of iteration for different TBQCP schemes ($a=0.5$, $b=1.0$) and the Krotov method for $\eta=6.4$. The amplitude of the initial negative linearly chirped control fields: (a) $A=0.015$ a.u. and (b) $A=0.06$ a.u.

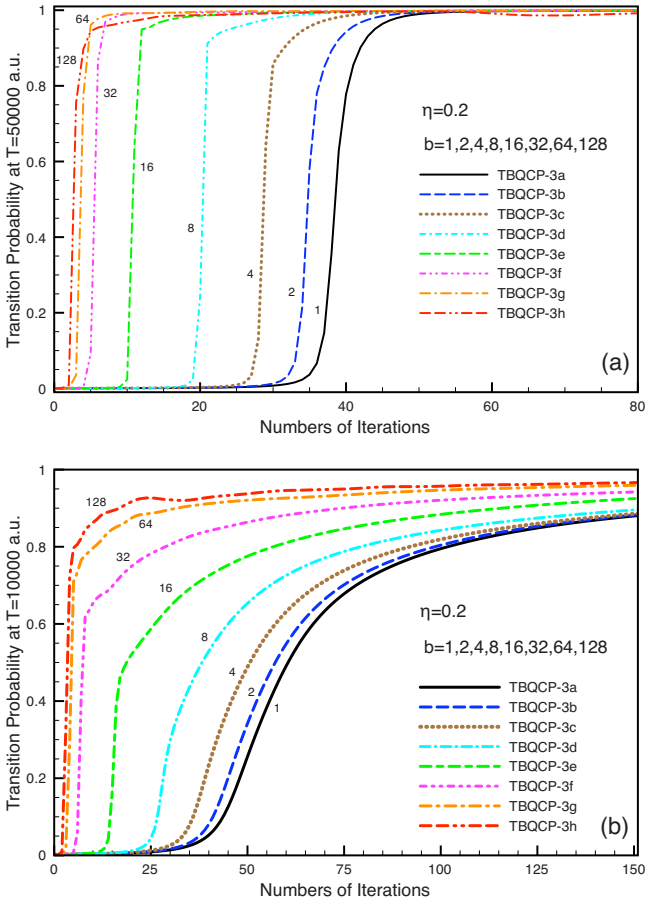


FIG. 7. (Color online) The transition probability $P_{0\to 15}(T)$ for (a) $T=50\,000$ a.u.($\sim 1.21$ ps) and (b) $T=10\,000$ a.u.($\sim 0.24$ ps), as a function of iteration for the TBQCP-3 scheme ($\eta=0.2$) for different $b$: 1.0 (TBQCP-3a), 2.0 (TBQCP-3b), 4.0 (TBQCP-3c), 8.0 (TBQCP-3d), 16.0 (TBQCP-3e), 32.0 (TBQCP-3f), 64.0 (TBQCP-3g), and 128.0 (TBQCP-3h). The amplitude of the initial negative linearly chirped control fields: (a) $A=0.015$ a.u. and (b) $A=0.06$ a.u.

simulations for the schemes TBQCP-2 and TBQCP-2n (as well as the simulations for TBQCP-3 and TBQCP-3n), starting with a moderate initial transition probability ($\sim 0.121$ at $n=0$), agree with each other well throughout the iterations. On the other hand, it is found in Fig. 1(b) that the transition probabilities $P_{0\to 15}(T)$ all rise quickly after 11 to 14 iterations (within 3 iterations of each other) from a very small initial transition probability ($\sim 0.00011$ at $n=0$). The good agreement shown in Figs. 1(a), and to a large degree in Fig. 1(b) (especially in the limit of $n \gg 1$), demonstrates that the numerically expedient schemes TBQCP-2 and TBQCP-3 maintain the same iterative monotonicity as do the TBQCP-2n and TBQCP-3n schemes, in spite of being derived in the limit of $\eta \to 0$ as well as $n \gg 1$. The same results (not shown) have also been found in simulations based on negative linearly chirped initial control fields. The remaining simulations have been carried out in terms of the TBQCP-1, TBQCP-2 and TBQCP-3 schemes, as well as the Krotov method [Eq. (28)].

The numerical calculations in Figs. 2 and 3 were performed with all three TBQCP schemes, as well as with the Krotov method, using $\eta=0.2$, $a=0.5$ and $b=1.0$. These simulations started with either (i) an LCT generated trial control field with $A=8.8$ a.u., corresponding to an initial transition probability of $P_{0\to 15}(T)=0.121$, and $T=50\,000$ a.u. or (ii) its filtered counterpart. All three TBQCP simulations possessed monotonically convergent behavior throughout the iterations, cf. Eq. (48). Figure 2 compares the results of the TBQCP schemes and the Krotov method. In the illustrations here the TBQCP schemes exhibit faster convergence behavior than the Krotov method, consistent with the mathematical analysis given in Sec. IV. The TBQCP-1 scheme has the fastest convergence rate in the first five iterations, which may arise due to its continuous monotonicity over time, cf. Eq. (22); the TBQCP-2 and TBQCP-3 scheme closely follow the convergence behavior of the TBQCP-1 scheme. As shown in Fig. 2(b), the TBQCP-3 scheme has the fastest convergence rate asymptotically (i.e., near the optimal global maximum), which may attributed to a larger acceleration parameter $2\eta$ adopted in the current TBQCP-3 simulations, compared to $\eta$ and $1.5\eta$ in the TBQCP-1 and TBQCP-2 simulations, respectively. The Krotov simulation provides a lower bound of the TBQCP simulations.

We have also performed control calculations to assess the effect of filtering using low and high cutoff frequencies $\omega_\ell = 0.005$ a.u. and $\omega_h = 0.05$ a.u., respectively, cf. Eq. (73). It was found in Figs. 2(a) and 2(b) that the inclusion of frequency filtering only slightly slows down the convergence rates; at the 300th iteration the unfiltered TBQCP-3 transition probability is $P_{0\to 15}(T)=0.999\,86$ and the filtered TBQCP-3 value is $P_{0\to 15}(T)=0.999\,36$, respectively. The control fields for both the unfiltered and filtered simulations closely resemble each other. Moreover, the effect of frequency filtering is minimal in both the TBQCP and Krotov approaches. The frequency filtering of the control fields effectively removes the DC component at the expense of slowing down the overall convergence rate throughout the iteration process, but filtering does not degrade the monotonic convergence behavior. The ubiquitous monotonically convergent behavior observed in Figs. 2(a) and 2(b) may be attributed to the fact that under mild assumptions the underlying transition probability control landscape contains only a global minimum (corresponding to zero transition probability) and a global maximum (corresponding to a transition probability equal to one) [32–35].

Figures 3(a)–3(c) show the windowed Fourier transform (WFT) power spectra of the unfiltered initial LCT generated control field, the final unfiltered TBQCP-3 control field, and the final filtered TBQCP-3 control field, respectively, corresponding to the converged results at the 300th iteration in Fig. 2(b). It was found that the final converged TBQCP-3 control fields not only engage earlier than the LCT generated initial field, but also contain additional strong lower frequency components corresponding to the transitions between the highly excited vibrational states. The unfiltered TBQCP-3 WFT power spectrum [Fig. 3(b)] also contains weak DC and very low frequency components. All cases show distinct chirping, although more complex structure is also present.

Figure 4(a) further compares the convergence behaviors of different TBQCP schemes as well as the Krotov method. Here we have considered two different values of $\eta$: 0.1 and 0.4. The control pulse length has been chosen as $T = 50\,000$ a.u. and the initial control field was generated by the LCT scheme, cf. Equation (70) with the parameter $A = 8.0$ a.u. It was found that the TBQCP schemes converge quicker than the Krotov method, especially for the larger $\eta$ value (here 0.4). Figure 4(b), based on the same LCT generated initial control field for Fig. 4(a), shows the convergence behavior of the TBQCP-3 scheme for different $b$ values ($b = 2.0$, 4.0, 8.0, 16.0, and 32.0) and for $\eta = 0.1$. The TBQCP-3 schemes stays monotonic over a wide range of $b$ values, but it becomes unstable near the transition probability maximum when $b$ becomes too large (here $b = 32.0$).

Figures 5 and 6 compare the convergence behavior of different TBQCP schemes and the Krotov method using negative linearly chirped initial control fields for two cases: (a) $A = 0.015$ a.u. and (b) $A = 0.006$ a.u. Here we have considered several different $\eta$ values (0.2, 0.4, and 0.8 in Fig. 5 and 6.4 in Fig. 6) and for two different control pulse lengths (a) $T = 50\,000$ a.u. and (b) $T = 10\,000$ a.u.($\sim 0.24$ ps). In addition, the parameters $a = 0.5$ [cf. Eq. (54)] and $b = 1.0$ [cf. Eq. (60)] were adopted for the TBQCP-2 and TBQCP-3 schemes, respectively. It is found that the TBQCP schemes perform better than the Krotov method, especially for large values of $\eta$ (here $\eta = 6.4$) and at the shorter pulse length $T$ (here $T = 10\,000$ a.u.), as clearly seen in Fig. 6(b). The difference in the takeoff among the TBQCP schemes (cf. Figure 5) is a manifestation of different iteration step sizes, $\eta$, $1.5\,\eta$ (corresponding to $a = 0.5$) and $2\,\eta$ (corresponding to $b = 1.0$), respectively, for the TBQCP-1, TBQCP-2, and TBQCP-3 schemes used in the simulations. All three TBQCP schemes, as well as the Krotov method, reach their respective maximum faster for larger $\eta$ values. However, the disparity between the TBQCP and Krotov results can be quite significant at the shorter pulse length (here $T = 10\,000$ a.u.), cf. Figures 5(b) and 6(b).

Finally, Fig. 7, corresponding to the same negative linearly chirped initial control fields adopted in Figs. 5 and 6, depicts the convergence behavior of the TBQCP-3 scheme for seven different $b$ values (2.0, 4.0, 8.0, 16.0, 32.0, 64.0, and 128.0), and for two different control pulse lengths (a) $T = 50\,000$ a.u. and (b) $T = 10\,000$ a.u., with a fixed value of $\eta = 0.2$. It was found that the TBQCP-3 scheme stays monotonic throughout the iterations over a wide range of $b$ values (here up to $b = 128.0$ for both $T = 50\,000$ a.u. and $T = 10\,000$ a.u.). The TBQCP-3 becomes unstable at $b = 128.0$ in the current simulations, as shown in the leftmost curves in Figs. 7(a) and 7(b). As revealed in Eq. (63), the TBQCP-3 scheme in the limit of $b \gg 1$, corresponding to a very large iteration step size, can cause a sudden rise of the transition probability of the target level (here $\nu' = 15$) in just a few iterations [it takes a mere 3 iterations to reach a transition probability $P_{0\to 15}(T)=0.756$ from $P_{0\to 15}(T)=0.00037$ for $T = 50\,000$ a.u., Figs. 7(a) and 4 iterations to reach $P_{0\to 15}(T)=0.724$ from $P_{0\to 15}(T)=0.0021$ for $T = 10\,000$ a.u., Fig. 7(b)].

## VII. SUMMARY

This paper presented various monotonically convergent iteration schemes for quantum control based on the TBQCP formulation derived from the Heisenberg equation of motion for a dynamical invariant of the observable. The TBQCP formulation is closely related to local control theory and can be implemented as fast convergent algorithms for tracking dynamical invariants. Moreover, it has been shown that TBQCP is related to various optimal control techniques, including the Krotov method and optimal control theory. This new paradigm may be adopted for solving a wide class of quantum control problems, and it may make more feasible the often computationally formidable study of multidimensional quantum control. It was shown that a simple implementation of TBQCP is efficient, and physically reasonable frequency filtering did not hinder the performance of TBQCP-based iteration procedures. Moreover, it was demonstrated that the TBQCP schemes can remain monotonically convergent over a wide range of iteration step parameters and control pulse lengths. The extensive flexibility associated with the TBQCP schemes, as well as the Krotov method, may be attributed to the underlying trap-free control landscape characteristic of the transition probability quantum

control dynamics [32–35]. The simulations in the paper demonstrated the efficiency of the TBQCP-based schemes in relation to the common Krotov method. A large scale comparison over a wide range of quantum systems, which is beyond the scope of this paper, will be needed to adequately assess features of these new TBQCP algorithms and other available methods. In making such comparisons it is important to keep in mind that virtually every method has a number of parameters that can only be chosen either judiciously or even by trial and error. Finally, the TBQCP method can be readily extended beyond the linear electric dipole formulation.

## ACKNOWLEDGMENTS

This work was partially supported by the Department of Energy. The authors are grateful to many fruitful discussions with Gabriel Turinici, Yukiyoshi Ohtsuki, and Jason Dominy.

## APPENDIX A: NUMERICAL IMPLEMENTATION OF $O^{(n)}(t)$ IN Eq. (46) AND $f_\mu^{(n+1)}(t)$ IN Eq. (44)

To facilitate the implementation of efficient and robust TBQCP iterative procedures, the positive semidefinite operator $O(T)=O_T$ is first diagonalized,

$$O(T) = \sum_k \sigma_k D|k\rangle\langle k|D^\dagger, \tag{A1}$$

where $\{\sigma_k \geq 0\}$ are the eigenvalues (assumed to be nondegenerate for simplicity. Thus, the largest eigenvalue is always greater than zero, i.e., $\max\{\sigma_1,\sigma_2,\ldots\}>0$) of $O(T)$, $D$ is a unitary matrix, i.e., $D^\dagger D=\mathbf{I}$, and $\{|k\rangle\}$ are the eigenstates of the field-free Hamiltonian $H_0$. At the $n$th iteration, the positive semidefinite dynamical invariant $O^{(n)}(t)$ associated with the control field $E^{(n)}(t)$ can be characterized by the same set of constant eigenvalues $\{\sigma_k\}$ and the corresponding instantaneous (adiabatic) eigenstates $\{|\varphi_k^{(n)}(t)\rangle\}$ satisfying the equation [39].

$$O^{(n)}(t)|\varphi_k^{(n)}(t)\rangle = \sigma_k|\varphi_k^{(n)}(t)\rangle, \tag{A2}$$

where $|\varphi_k^{(n)}(t)\rangle$ is a solution of the time-dependent equation

$$\frac{\partial}{\partial t}|\varphi_k^{(n)}(t)\rangle = \frac{1}{\imath\hbar}\{H_0 - \mu E^{(n)}(t)\}|\varphi_k^{(n)}(t)\rangle, \tag{A3}$$

subject to the boundary condition $|\varphi_k^{(n)}(T)\rangle=D|k\rangle$. Since $O^{(n)}(t)$ can be written as

$$O^{(n)}(t) = U_n(t,T)O(T)U_n^\dagger(t,T), \tag{A4}$$

where

$$\frac{\partial}{\partial t}U_n(t,T) = \frac{1}{\imath\hbar}\{H_0 - \mu E^{(n)}(t)\}U_n(t,T), \quad U_n(T,T)=\mathbf{I}, \tag{A5}$$

we find that

$$\begin{aligned} O^{(n)}(t)[U_n(t,T)D|k\rangle] &= U_n(t,T)O(T)U_n(T,t)U_n(t,T)D|k\rangle \\ &= U_n(t,T)D\left(\sum_\ell \sigma_\ell|\ell\rangle\langle\ell|\right)D^\dagger D|k\rangle \\ &= \sigma_k[U_n(t,T)D|k\rangle], \end{aligned} \tag{A6}$$

giving rise to the eigenstates

$$|\varphi_k^{(n)}(t)\rangle = U_n(t,T)D|k\rangle = U_n(t,T)|\varphi_k^{(n)}(T)\rangle = U_n(t,0)|\varphi_k^{(n)}(0)\rangle, \tag{A7}$$

with $|\varphi_k^{(n)}(T)\rangle=D|k\rangle$. Using the above relations, we immediately derive that

$$\langle\varphi_k^{(n)}(t)|\varphi_\ell^{(n)}(t)\rangle = \langle k|D^\dagger U_n(T,t)U_n(t,T)D|\ell\rangle = \langle k|\ell\rangle = \delta_{k\ell}, \tag{A8}$$

assuring that the eigenstates $\{|\varphi_k^{(n)}(t)\rangle\}$ are orthogonal throughout time. From Eqs. (A1) and (A7), the dynamical invariant $O^{(n)}(t)$ can be expanded as

$$O^{(n)}(t) \equiv U_n(t,T)O(T)U_n^\dagger(t,T) = \sum_k \sigma_k|\varphi_k^{(n)}(t)\rangle\langle\varphi_k^{(n)}(t)|, \tag{A9}$$

together with the identity relation

$$\sum_k |\varphi_k^{(n)}(t)\rangle\langle\varphi_k^{(n)}(t)| = U_n(t,T)D\left(\sum_k |k\rangle\langle k|\right)D^\dagger U_n(T,t) = \mathbf{I}. \tag{A10}$$

The expectation value $\langle O^{(n)}(t)\rangle$ can be written as

$$\begin{aligned} \langle O^{(n)}(t)\rangle &= \langle\psi^{(n+1)}(t)|O^{(n)}(t)|\psi^{(n+1)}(t)\rangle \\ &= \sum_k \sigma_k|\langle\varphi_k^{(n)}(t)|\psi^{(n+1)}(t)\rangle|^2 \geq 0, \end{aligned} \tag{A11}$$

which in turns yields the inequality

$$\begin{aligned} \langle O(t)\rangle &\leq \max\{\sigma_1,\sigma_2,\ldots\}\sum_k |\langle\varphi_k^{(n)}(t)|\psi^{(n+1)}(t)\rangle|^2 \\ &= \max\{\sigma_1,\sigma_2,\ldots\}, \end{aligned} \tag{A12}$$

since, from Eq. (A10),

$$\sum_k |\langle\varphi_k^{(n)}(t)|\psi^{(n+1)}(t)\rangle|^2 = 1. \tag{A13}$$

From Eqs. (20) and (A12), it is readily seen that the iteration scheme based on Eq. (43) converges asymptotically as follows:

$$\lim_{n\to\infty}\langle O^{(n)}(T)\rangle \to \max\{\sigma_1,\sigma_2,\ldots\}. \tag{A14}$$

By substituting Eq. (A9) into Eq. (44), we have

$$\begin{aligned} f_\mu^{(n+1)}(t) = -\frac{2}{\hbar}\mathrm{Im}\Bigg\{\sum_k \sigma_k\langle\psi^{(n+1)}(t)|\varphi_k^{(n)}(t)\rangle \\ \times\langle\varphi_k^{(n)}(t)|\mu|\psi^{(n+1)}(t)\rangle\Bigg\}. \end{aligned} \tag{A15}$$

At each iteration, Eqs. (A11) and (A15) can be quickly computed by first propagating $|\varphi_k^{(n)}(t)\rangle$ backward, starting at

$|\varphi_k^{(0)}(T)\rangle$, and then $|\psi^{(n+1)}(t)\rangle$ forward, starting at $|\psi^{(n+1)}(0)\rangle$ [for example, using the second-order split-operator technique] to solve Eqs. (A3) and (47). For multidimensional quantum systems in the coordinate representation, it may be prudent to first compute $|\varphi_k^{(n)}(0)\rangle = U_n(0,T)|\varphi_k^{(n)}(T)\rangle$ (at small overhead), then integrate both $|\varphi_k^{(n)}(t)\rangle$ and $|\psi^{(n+1)}(t)\rangle$ forward to avoid the large overhead of storing the time-dependent dynamical invariant eigenstates $|\varphi_k^{(n)}(t)\rangle$ over the whole time interval $t \in [0,T]$.

## APPENDIX B: EVALUATION OF THE CONTROL FIELD $E^{(n+1)}(t)$ AT THE $(n+1)$th ITERATION

The TBQCP control field $E^{(n+1)}(t)$, $t \in [0,T]$, at the $(n+1)$th iteration is updated using the recurrence relation

$$E^{(n+1)}(t_i) = E^{(n)}(t_i) + (1-\zeta^{(n+1)})\eta S(t_i) f_\mu^{(n+1)}(t_i) + \eta S(t_i) f^{(n+1)}(t_i), \quad i = 1,2,\ldots,\boldsymbol{M}, \tag{B1}$$

where $\zeta^{(1)}=0$ and $f^{(1)}(t)=0$ and

$$\begin{cases} \zeta^{(n+1)} = 0, \quad f^{(n+1)}(t_i) = 0 & \text{(TBQCP-1)} \\ \zeta^{(n+1)} = -a, \quad \eta S(t) f^{(n+1)}(t_i) = -a[E^{(n)}(t_i) - E^{(n-1)}(t_i)], \quad 0 < a \le 1 & \text{(TBQCP-2)} \\ \zeta^{(n+1)} = -b, \quad f^{(n+1)}(t_i) = -b f_\mu^{(n)}(t_i), \quad b > 0 & \text{(TBQCP-3)} \end{cases}$$

if $n \ge 1$. Here the time interval $[0,T]$ has been discretized into $\boldsymbol{M}$ evenly spaced grid points. To compute

$$f_\mu^{(n+1)}(t_i) = -\frac{2}{\hbar}\mathrm{Im}\langle\psi^{(n+1)}(t_i)|\varphi_{\nu'}^{(n)}(t_i)\rangle\langle\varphi_{\nu'}^{(n)}(t_i)|\mu|\psi^{(n+1)}(t_i)\rangle \tag{B2}$$

in Eq. (B1), we first store

$$\langle r|\varphi_{\nu'}^{(n)}(t_i)\rangle = \langle r|U_n(t_i,t_{i+1})\ldots U_n(t_{M-2},t_{M-1})U_n(t_{M-1},T)|\nu'\rangle, \tag{B3}$$

$i=M-1,M-2,\ldots,1,0$, utilizing the backward propagator

$$U_n(t_i,t_{i+1}) \approx \exp\left(\frac{\imath}{\hbar}\{H_0 - \mu E^{(n)}(t_i)\}\Delta t\right), \tag{B4}$$

followed by the evaluation of

$$\langle r|\psi^{(n+1)}(t_i)\rangle = \langle r|U_{n+1}(t_i,t_{i-1})\ldots U_{n+1}(t_2,t_1)U_{n+1}(t_1,0)|\nu\rangle, \tag{B5}$$

facilitated using the forward propagator

$$U_{n+1}(t_i,t_{i-1}) \approx \exp\left(-\frac{\imath}{\hbar}\{H_0 - \mu E^{(n+1)}(t_{i-1})\}\Delta t\right). \tag{B6}$$

Alternatively, we may first compute $\langle r|\varphi_{\nu'}^{(n)}(0)\rangle$ using Eq. (B3), followed by the simultaneous evaluation of

$$\langle r|\varphi_{\nu'}^{(n)}(t_i)\rangle = \langle r|U_n(t_i,t_{i-1})\ldots U_n(t_2,t_1)U_n(t_1,0)|\varphi_{\nu'}^{(n)}(0)\rangle \tag{B7}$$

and

$$\langle r|\psi^{(n+1)}(t_i)\rangle = \langle r|U_{n+1}(t_i,t_{i-1})\ldots U_{n+1}(t_2,t_1)U_{n+1}(t_1,0)|\nu\rangle \tag{B8}$$

for $i=1,2,\ldots,M$, leading to Eq. (B2), where the forward propagator is

$$U_n(t_i,t_{i-1}) \approx \exp\left(-\frac{\imath}{\hbar}\{H_0 - \mu E^{(n)}(t_{i-1})\}\Delta t\right). \tag{B9}$$

This latter implementation is advantageous when the storage of the time-dependent dynamical invariant eigenfunction $\langle r|\varphi_{\nu'}^{(n)}(t)\rangle$ over the time interval $[0,T]$ becomes problematic, for example, when the number of grid points in the $r-t$ plane becomes too large. The forward propagator $U_n(t_i,t_{i-1})$ was evaluated using a short-time second-ordered split-operator scheme [51–54]

$$\begin{aligned} U_n(t_i,t_{i-1}) &\approx \exp\left(-\frac{\imath}{\hbar}H^{(n)}(t_{i-1})\Delta t\right) \\ &\approx \exp\left(-\frac{\imath}{2\hbar}K\Delta t\right)\exp\left(-\frac{\imath}{\hbar}\{V - \mu E^{(n)}(t_{i-1})\}\Delta t\right) \\ &\quad \times \exp\left(-\frac{\imath}{2\hbar}K\Delta t\right), \end{aligned} \tag{B10}$$

for $i=1,2,\ldots,M \gg 1$, $\Delta t = T/M$, and $H^{(n)}(t) = H_0 - \mu E^{(n)}(t) = K + V - \mu E^{(n)}(t)$, with $K$ and $V$ being the kinetic energy and potential energy operators, respectively. The backward propagator $U_n(t_i,t_{i+1})$ was evaluated using the relation $U_n(t_i,t_{i+1}) = U_n^\dagger(t_{i+1},t_i)$. Moreover, a damping function of the form [51]

$$F(r_i) = \sin\left(\frac{\pi}{2}\frac{r_{\mathrm{mask}} + \Delta r_{\mathrm{mask}} - r_i}{\Delta r_{\mathrm{mask}}}\right) \quad r_i \ge r_{\mathrm{mask}}, \tag{B11}$$

was introduced, where $r_{\mathrm{mask}} = 14.7$ a.u. (compared to the location of the last spatial grid point at $r_{\max} = 15$ a.u. in the calculations) is the position at which the damping function takes effect and $\Delta r_{\mathrm{mask}} = r_{\max} - r_{\mathrm{mask}} = 0.3$ a.u. is the range

over which the damping function was applied. This procedure is equivalent to adding a negative imaginary potential at the far end of the spatial grid to prevent the artificial reflection of the propagating wave function. Thus, the time-dependent quantum states $|\psi^{(n+1)}(t)\rangle$ and $|\varphi^{(n)}(t)\rangle$ were effectively expressed as $\langle r|\psi^{(n+1)}(t)\rangle = \langle r|\psi^{(n+1)}(t)\rangle$, $\langle r|\varphi^{(n)}(t)\rangle = \langle r|\varphi^{(n)}(t)\rangle$ if $r < r_{\text{mask}}$ and $\langle r|\psi^{(n+1)}(t)\rangle = \langle r|\psi^{(n+1)}(t)\rangle F(r)$, $\langle r|\varphi^{(n)}(t)\rangle = \langle r|\varphi^{(n)}(t)\rangle F(r)$ if $r \geq r_{\text{mask}}$.


[1] A. M. Weiner, Rev. Sci. Instrum. **71**, 1929 (2000).
[2] A. P. Peirce, M. A. Dahleh, and H. Rabitz, Phys. Rev. A **37**, 4950 (1988).
[3] S. Shi, A. Woody, and H. Rabitz, J. Chem. Phys. **88**, 6870 (1988).
[4] R. Kosloff, S. A. Rice, P. Gaspard, S. Tersigni, and D. J. Tannor, Chem. Phys. **139**, 201 (1989).
[5] S. Rice and M. Zhao, *Optical Control of Molecular Dynamics* (Wiley, New York, 2000).
[6] J. Werschnik and E. K. U. Gross, J. Phys. B **40**, R175 (2007).
[7] A. Assion, T. Baumert, M. Bergt, T. Brixner, B. Kiefer, V. Seyfried, M. Strehle, and G. Gerber, Science **282**, 919 (1998).
[8] T. C. Weinacht, J. L. White, and P. H. Bucksbaum, J. Phys. Chem. A **103**, 10166 (1999).
[9] R. Bartels, S. Backus, E. Zeek, L. Misoguti, G. Vdovin, I. P. Christov, M. M. Murnane, and H. C. Kapteyn, Nature (London) **406**, 164 (2000).
[10] M. Wollenhaupt, V. Engel, and T. Baumert, Annu. Rev. Phys. Chem. **56**, 25 (2005).
[11] R. Kosloff, A. D. Hammerich, and D. Tannor, Phys. Rev. Lett. **69**, 2172 (1992).
[12] D. J. Tannor, R. Kosloff, and A. Bartana, Faraday Discuss. **113**, 365 (1999).
[13] V. Engel, C. Meier, and D. J. Tannor, Adv. Chem. Phys. **141**, 29 (2009).
[14] M. Sugawara and Y. Fujimura, Chem. Phys. **196**, 113 (1995).
[15] Y. Ohtsuki, Y. Yahata, H. Kono, and Y. Fujimura, Chem. Phys. Lett. **287**, 627 (1998).
[16] M. Sugawara, J. Chem. Phys. **118**, 6784 (2003).
[17] M. Mirrahimi, G. Turinici, and P. Rouchon, J. Phys. Chem. A **109**, 2631 (2005).
[18] A. Rothman, T.-S. Ho, and H. Rabitz, Phys. Rev. A **72**, 023416 (2005).
[19] A. Rothman, T.-S. Ho, and H. Rabitz, J. Chem. Phys. **123**, 134104 (2005).
[20] A. Rothman, T.-S. Ho, and H. Rabitz, Phys. Rev. A **73**, 053401 (2006).
[21] R. S. Judson and H. Rabitz, Phys. Rev. Lett. **68**, 1500 (1992).
[22] A. Borzì, J. Salomon, and S. Volkwein, J. Comput. Appl. Math. **216**, 170 (2008).
[23] S. E. Sklarz and D. J. Tannor, Phys. Rev. A **66**, 053619 (2002).
[24] J. P. Palao and R. Kosloff, Phys. Rev. A **68**, 062308 (2003).
[25] J. P. Palao, R. Kosloff, and C. P. Koch, Phys. Rev. A **77**, 063412 (2008).
[26] W. Zhu, J. Botina, and H. Rabitz, J. Chem. Phys. **108**, 1953 (1998).
[27] W. Zhu and H. Rabitz, J. Chem. Phys. **109**, 385 (1998).
[28] W. Zhu and H. Rabitz, J. Chem. Phys. **110**, 7142 (1999).
[29] Y. Maday and G. Turinici, J. Chem. Phys. **118**, 8191 (2003).
[30] Y. Ohtsuki, G. Turinici, and H. Rabitz, J. Chem. Phys. **120**, 5509 (2004).
[31] J. Salomon and G. Turinici, J. Chem. Phys. **124**, 074102 (2006).
[32] H. Rabitz, M. Hsieh, and C. Rosenthal, Science **303**, 1998 (2004).
[33] H. Rabitz, T.-S. Ho, M. Hsieh, R. Kosut, and M. Demiralp, Phys. Rev. A **74**, 012721 (2006).
[34] Z. Shen, M. Hsieh, and H. Rabitz, J. Chem. Phys. **124**, 204106 (2006).
[35] T.-S. Ho and H. Rabitz, J. Photochem. Photobiol., A **180**, 226 (2006).
[36] Y. Ohtsuki, Y. Teranishi, P. Saalfrank, G. Turinici, and H. Rabitz, Phys. Rev. A **75**, 033407 (2007).
[37] Y. Ohtsuki and K. Nakagami, Phys. Rev. A **77**, 033414 (2008).
[38] M. Lapert, R. Tehini, G. Turinici, and D. Sugny, Phys. Rev. A **78**, 023408 (2008).
[39] J. H. R. Lewis and W. B. Riesenfeld, J. Math. Phys. **10**, 1458 (1969).
[40] P. Gross, H. Singh, H. Rabitz, K. Mease, and G. M. Huang, Phys. Rev. A **47**, 4593 (1993).
[41] Y. Chen, P. Gross, V. Ramakrishna, H. Rabitz, and K. Mease, J. Chem. Phys. **102**, 8001 (1995).
[42] Y. Chen, P. Gross, V. Ramakrishna, H. Rabitz, K. Mease, and H. Singh, Automatica **33**, 1617 (1997).
[43] W. Zhu, M. Smit, and H. Rabitz, J. Chem. Phys. **110**, 1905 (1999).
[44] W. Zhu and H. Rabitz, J. Chem. Phys. **119**, 3619 (2003).
[45] S. W. Roberts, Technometrics **1**, 239 (1959).
[46] S. W. Roberts, Technometrics **8**, 411 (1966).
[47] S. V. Crowder, Technometrics **29**, 401 (1987).
[48] J. M. Lucas and M. S. Saccucci, Technometrics **32**, 1 (1990).
[49] S. Butterworth, Exp. Wirel. Wirel. Eng. **7**, 536 (1930).
[50] W. H. Press, S. A. Teukolsky, W. T. Vetterling, and B. P. Flannery, *Numerical Recipes in Fortran*, 2nd ed. (Cambridge University Press, New York, 1992).
[51] S. Mahapatra and N. Sathyamurthy, J. Chem. Soc., Faraday Trans. **93**, 773 (1997).
[52] Y. Maday, J. Salomon, and G. Turinici, Numer. Math. **103**, 323 (2006).
[53] Y. Maday, J. Salomon, and G. Turinici, SIAM (Soc. Ind. Appl. Math.) J. Numer. Anal. **45**, 2468 (2007).
[54] M. Belhadj, J. Salomon, and G. Turinici, J. Phys. A: Math. Theor. **41**, 362001 (2008).